RESEARCH ARTICLE | DECEMBER 11 2024

Success and failure in mayonnaise preparation in the kitchen

Special Collection: Kitchen Flows 2024

Mahdiyeh Ghaffari ; Arjen Bot ; Rogier Brussee ; Gerjen H. Tinnevelt ; Jeroen J. Jansen

Physics of Fluids 36, 124123 (2024)
https://doi.org/10.1063/5.0245176

Physics of Fluids ARTICLE pubs.aip.org/aip/pof

Success and failure in mayonnaise preparation in the kitchen

Cite as: Phys. Fluids **36**, 124123 (2024); doi: 10.1063/5.0245176
Submitted: 24 October 2024 · Accepted: 18 November 2024 ·
Published Online: 11 December 2024

Mahdiyeh Ghaffari,[1,a)] Arjen Bot,[2,3] Rogier Brussee,[4] Gerjen H. Tinnevelt,[1] and Jeroen J. Jansen[1]

AFFILIATIONS

[1]Analytical Chemistry, Institute for Molecules and Materials, Radboud University, P.O. Box 9010, 6500 GL Nijmegen, The Netherlands
[2]Unilever Foods Innovation Centre, Bronland 14, NL-6708 WH Wageningen, The Netherlands
[3]Laboratory of Physics and Physical Chemistry of Foods, Department of Agrotechnology and Food Sciences, Wageningen University and Research, Bornse Weilanden 9, NL-6708 WG Wageningen, The Netherlands
[4]Jheronimus Academy of Data Science, Sint Janssingel 92, NL-5211 DA 's Hertogenbosch, The Netherlands

Note: This paper is part of the Special Topic: Kitchen Flows 2024.
[a)]**Author to whom correspondence should be addressed:** mahdiyeh.ghaffari@ru.nl

ABSTRACT

The combination of near-infrared spectroscopic techniques (HSI or hyperspectral imaging) with advanced image analysis allows noninvasive, quantitative analysis of slow mixing phenomena. This is illustrated in a small study to monitor the preparation of homemade mayonnaise, specifically concerning the major challenge of "breaking" the emulsion. The context of the phenomenon in terms of the physics of mixing is explained as well. This study demonstrates that the Kullback–Leibler divergence metric, when applied to HSI data, enables quantitative tracking of emulsion mixing dynamics and can be used to quantify emulsion homogeneity and identify phase inversion during mayonnaise preparation if manual oil addition proceeds too quickly. This approach holds promise for real-time monitoring of emulsion quality in industrial settings where the state of the emulsion cannot always be determined visually.

I. INTRODUCTION

Patience is a virtue, in life and in the kitchen. Nowhere is this proverb demonstrated better than during manual preparation of mayonnaise. Mayonnaise is a high internal phase oil-in-water emulsion (HIPE), in which the fraction of dispersed oil can be close to 80%. It goes without saying that preparing such an emulsion is a bit of an art. In particular, the rate of oil addition compared to the rate of mixing is critical.[1] If the oil is added too quickly, the emulsion will invert (or "break"), and a low-viscosity slurry will remain. If the oil is added sufficiently slow, the emulsion will remain water-continuous, and a pasty condiment will be obtained (see Fig. 1). The impatient will be punished!

The present paper studies a novel methodology for quantifying observations in the preparation of high-internal phase emulsions, such as mayonnaise. It should be noted that the mayonnaise case is just an example, and the technique can be applied in the study of slow mixing phenomena in general.

To introduce the effect, first some background concerning the physics of this interesting mixing problem is provided. Two independent phenomena are involved. The first one can be explained in terms of the (qualitative) Krieger–Dougherty equation, which states that the viscosity η of a (water-in-oil) emulsion increases with the amount of dispersed oil,

$$\eta = \eta_{cont}\left(1 - \frac{\varphi}{\varphi_{cp}}\right)^{-K\varphi_{cp}}, \tag{1}$$

where η_{cont} is the viscosity of the continuous phase, φ is the volume fraction of the dispersed phase, φ_{cp} is the maximum packing fraction of the dispersed phase, and K is a constant that should be 5/2 to retrieve the Einstein equation for the viscosity of a dilute suspension of hard spheres[2]

$$\eta = \eta_{cont}\left(1 + \frac{5}{2}\varphi\right). \tag{2}$$

The Krieger–Dougherty equation expresses the observation that the viscosity increases steeply and in a very non-linear way when the packing fraction of the droplets approaches close packing, typically taken to

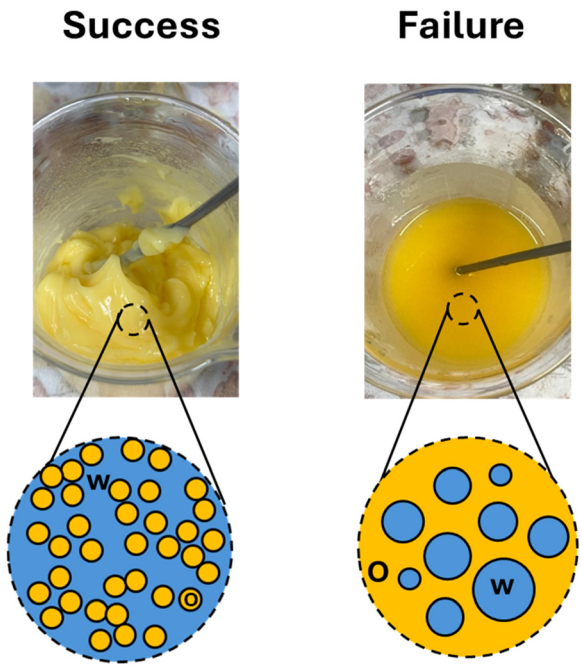

FIG. 1. Demonstrations of a successful preparation of mayonnaise (left image, slow addition of oil) and a failed attempt (right image, rapid addition of oil). The trials are explained later in the text in more detail.

be about 0.7, but depending on the monodispersity and the deformability of the droplets.[3]

The second phenomenon involves the capillary number Ca, governing the breakup of droplets in emulsification,

$$Ca = \frac{\eta_{cont}\dot{\gamma}d}{2\gamma}, \tag{3}$$

where $\dot{\gamma}$ is the shear rate, d is the droplet diameter, and γ is the surface tension. The critical capillary number Ca_{cr} is the value of the capillary number to be exceeded for droplet breakup to occur. The shape of the curve for the critical capillary number depends on flow type and viscosity ratio r_v

$$r_v = \frac{\eta_{disp}}{\eta_{cont}}, \tag{4}$$

where η_{disp} is the viscosity of the dispersed fluid and is shown in Fig. 2. There are multiple mechanisms known by which droplets may break.[4,5] In elongational flow, the smallest droplets are achieved at high r_v whereas there is an optimum ratio for shear flow (because of the rotational component of shear flow). Ca/Ca_{cr} determines whether one should expect a binary breakup of the droplets (Ca/Ca_{cr} approximately 1) or breakup in long filaments due to Rayleigh instabilities (higher Ca/Ca_{cr}). The viscosity ratio of vegetable oil and egg yolk is typically in the range of 0.01–0.1, in the range where Ca_{cr} does not depend too steeply on r_v (see Fig. 2). Here, it is possible to mix in the vegetable oil as small droplets in the egg yolk. As the amount of dispersed phase increases, the viscosity of the emulsion increases as well [because of Eq. (1)]. However, if the oil is added too suddenly (or in too large portions),

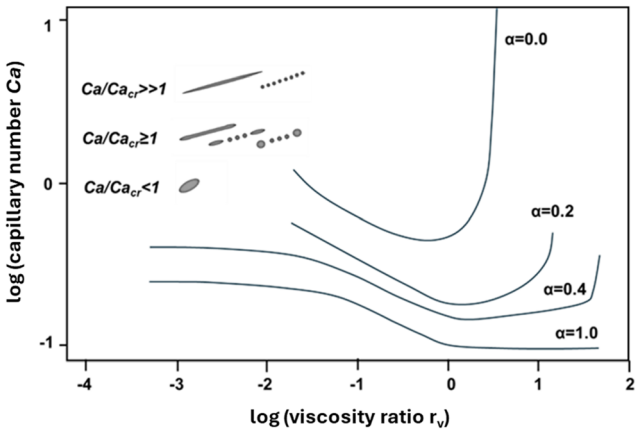

FIG. 2. Critical capillary number Ca_{cr} as a function of viscosity ratio r_v, according to Refs. 6 and 3 in pure shear ($\alpha = 0$) and pure elongation flow ($\alpha = 1$). Droplet breakup during whisking resembles breakup in shear flow more than in elongational flow. Different breakup mechanisms may apply, depending on the ratio of Ca and Ca_{cr}. The typical viscosity ratio of vegetable oil and egg yolk is ~0.01–0.1.

the high-viscosity emulsion can be found in large pools of relatively low-viscosity oil ($r_v > 10$). Since whisking resembles shear flow more than elongational flow, this means we enter a regime where Ca_{cr} becomes very large—or in other words, the droplets become very large [as a consequence of Eq. (1)], effectively meaning that it is impossible to create further fine emulsion droplets. Since the size of the emulsion droplets ultimately determines the consistency of the condiment due to the Laplace pressure of the droplets that determines their resistance against deformation,[4,5] this means it is impossible in that situation to attain the required consistency or even a stable emulsion.

In summary, two fundamental mixing-related phenomena can be seen to have a direct impact on the success of making a sauce in the kitchen. This will be demonstrated in the present experiment by increasing the size of the portions of oil added to the mixture in a single go in-between mixing steps. These experiments will demonstrate how hyperspectral imaging (HSI) techniques can be used to study such slow mixing phenomena.

This study employs near-infrared HSI[7–10] as a key technique, which provides noninvasive, label-free chemical identification of components, thereby eliminating potential interference from labeling agents. By capturing detailed spectral information across a broad wavelength range, HSI allows for an analysis of both the emulsion's spatial distribution of different ingredients. We use multivariate curve resolution with alternating least squares (MCR-ALS)[10] and principal component analysis (PCA)[11] to decompose and visualize the hyperspectral data to identify the abundance of each ingredient per pixel. We then use the Kullback–Leibler relative (information) entropy to quantify the divergence of the emulsion from homogeneity at different length scales as well as the characteristics of the droplets in the emulsion. This combined approach enables a detailed examination of droplet size distributions, phase inversion, and overall emulsion stability under varying preparation conditions, giving a handle on the fundamental dynamics of high-internal phase emulsions. We also discuss how these techniques could be used as a basis for the design of a sensor to monitor emulsion stability in an industrial setting.

TABLE I. The experimental conditions are summarized.

Trial number	Oil portions	Oil (g)	Yolk (g)	Vinegar (g)	Emulsion type
1	40 × 5 g	200	20	30	O/W
2	20 × 10 g	200	20	30	O/W
3	10 × 20 g	200	20	30	W/O
4	6 × 30 g + 1 × 20 g	200	20	30	W/O
5	5 × 40 g	200	20	30	W/O
6	4 × 50 g	200	20	30	W/O
7	1 × 200 g	200	20	30	W/O

II. MATERIALS AND METHODS

A. Experimental

Seven distinct trials were conducted to investigate the oil and water emulsification. Slow or rapid addition of oil was simulated by adding smaller or bigger portions of oil. Each trial started with 20 g of egg yolk, followed by the addition of 200 g of olive oil, and concluded with 30 g of white vinegar added at the end. We varied the method of oil incorporation between trials. In the first trial, the 200 g of oil was added incrementally in 40 steps of 5 g each, with thorough manual mixing performed after each addition. In contrast, the seventh trial involved the addition of the entire 200 g of oil in a single step, followed by prolonged manual mixing. The final step in each trial was the addition of 30 g of white vinegar and mixing before image collection. A summary of the experimental conditions is provided in Table I. RGB images for the prepared samples for trial 1 and trial 7 are presented in Fig. 1. In addition, two binary mixture samples were prepared by combining oil and yolk, and oil and vinegar, in a 1:1 ratio.

The sample is imaged using, i.e., scanned line-by-line by moving[12–14] either the imaging system or the sample along a unidirectional path, while the imaging system captures spectral data of a row of pixels.[7,15–19] For each trial, a portion of the prepared sample was transferred to a sample holder and positioned on the HSI camera. As the sample holder moved in a controlled manner, the hyperspectral camera collected spectral images sequentially along the scanned line. This process generated a detailed hyperspectral image, with each line of data contributing to the spatial and spectral representation of the entire sample. This method ensures precise measurement of the sample's properties while minimizing motion artifacts. This approach produces 3D data consisting of two spatial and one spectral dimension, offering a comprehensive view of the sample's properties across both spatial and spectral domains as presented in Fig. 3.

To measure the datasets in this study, we utilized the SPECIM FX17, a camera from Specim, Oulu, Finland, hyperspectral imaging system equipped with a macro lens. This system operates within a wavelength range of 900–1700 nm, providing a spatial resolution of 15 × 15 μm per pixel. The images generated in this study have dimensions of 640 pixels by 1100 pixels. For a typical image, the acquisition time is approximately 30 s.

B. Data analysis

Typically, HSI represents a composite signal gathered from the sample by the detector.[20] To address this, signal unmixing techniques

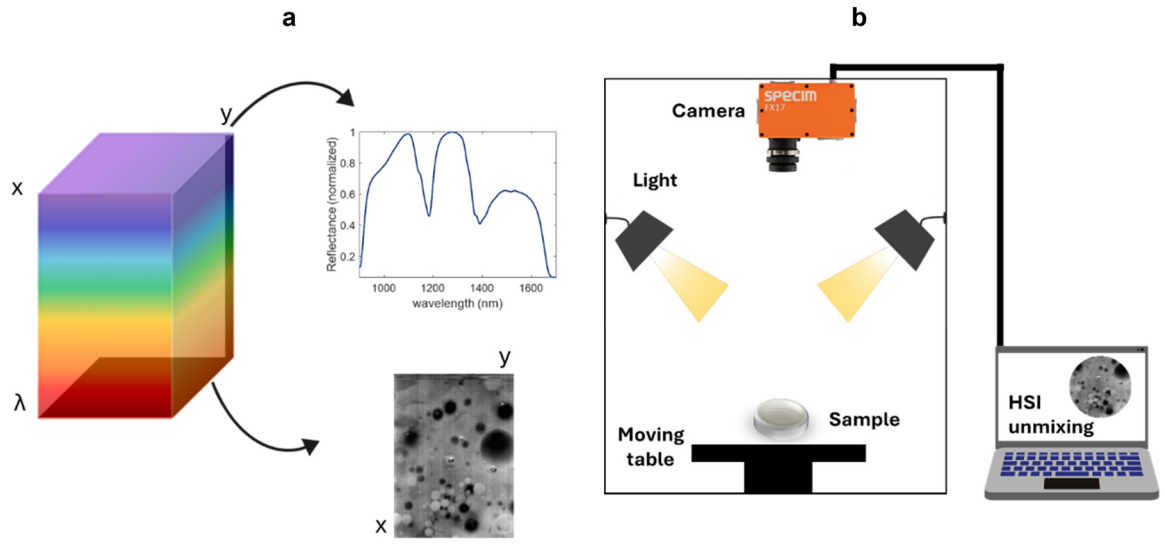

FIG. 3. (a) The general schematic of a hyperspectral image, which comprises two spatial dimensions (x and y) and one spectral dimension (λ). (b) Schematic of the hyperspectral imaging setup used for collecting the images.

are essential for decomposing the mixed signals into constituent components that correspond to different ingredients of the sample.[21] Principal component analysis (PCA) and multivariate curve resolution with alternating least squares (MCR-ALS) are employed for visualization and signal unmixing, facilitating the differentiation and detailed analysis of individual components within the emulsion.[22]

Principal Component Analysis (PCA) is a powerful technique used to visualize HyperSpectral Imaging (HSI) data of mayonnaise in an abstract space. By reducing the dimensionality of complex HSI data, PCA effectively represents key spectral variations in a simplified form, making it easier to interpret and analyze. In HSI, datasets are structured as three-way arrays denoted as $\widetilde{\mathbf{R}}$, indexed by x, y, and λ where x and y represent the spatial dimensions, and λ represents the spectral dimension. To facilitate bilinear decomposition, the three-way array $\widetilde{\mathbf{R}}$ is unfolded into a two-dimensional matrix $\mathbf{R}$, indexed by the pair (x, y) and λ defined as

$$\mathbf{R} = \text{unfold}\,(\widetilde{\mathbf{R}}). \tag{5}$$

This unfolding process isolates the spectral profiles in one mode and the spatial pixels in another, enabling the subsequent generation of a bilinear matrix.

To perform PCA, singular value decomposition (SVD) is commonly used. SVD decomposes the data matrix $\mathbf{R}$ to three components: the left singular vectors $\mathbf{U}$, the right singular vectors $\mathbf{V}$, and the singular values $\mathbf{D}$. Specifically, the scores ($\mathbf{SC}$) are computed as $\mathbf{SC} = \mathbf{U} \times \mathbf{D}$, where $\mathbf{SC}$ represents the weighted scores. Each row in $\mathbf{SC}$ corresponds to a pixel in the original dataset, and each score encapsulates a specific characteristic of that pixel such as variations in its chemical composition or spectral signature. By plotting these scores, one can extract insightful information about underlying patterns, including component correlations, spatial clustering, and compositional trends across regions within the data or visualize the complex HSI data in a more accessible and interpretable form. This approach is particularly useful for identifying spatial and spectral variations within mayonnaise samples, providing a clear and concise method for analyzing high-dimensional data in food quality studies.

Multivariate Curve Resolution can decompose a hyperspectral image which is structured as an array of intensities per wavelength (or more precisely, wavelength interval of fixed length) for each pixel, i.e., $\mathbf{R}$. To perform a spectral decomposition, it is assumed that at each pixel, the signal is a mixture of signals, each of which is proportional to the concentration of different ingredients at that pixel; that is, the signal is decomposed as

$$\mathbf{R} = \sum\nolimits_n \mathbf{CS}^{\mathrm{T}} + \mathbf{E}, \tag{6}$$

where n is the number of different ingredients, $\mathbf{S}^{\mathrm{T}}$ is the spectral profiles of n ingredients, $\mathbf{C}$ is the concentration or volume fraction of the n ingredients at different pixels, where $\mathbf{E}$ is the remainder for each pixel for each different wavelength (interval) considered as an error term. The goal is to minimize some functional $L(\mathbf{R}, \mathbf{E})$ aggregating error contributions over all pixels and wavelengths.

Multivariate Curve Resolution-Alternating Least Squares (MCR-ALS) is a widely utilized data unmixing technique that facilitates the decomposition of a bilinear system into pure chemical information. For this, the matrix $\mathbf{R}$ is considered with rows indexed by the pixel (x, y) and the columns by λ. Likewise, the matrix $\mathbf{C}$ is considered as a matrix with rows indexed by the pixel (x, y) and the columns by the ingredients n, $\mathbf{S}^{\mathrm{T}}$ contains the pure spectral profiles of n ingredients and $\mathbf{E}$ as a matrix whose rows are indexed by the pixel the pixel (x, y) and whose columns are indexed by λ. Equation (6) then becomes a matrix factorization problem,

$$\mathbf{R} = \mathbf{CS}^{\mathrm{T}} + \mathbf{E}, \tag{7}$$

where the aim is to minimize the error functional $\mathrm{L}(\mathbf{R}, \mathbf{E})$. However, this cannot uniquely define $\mathbf{C}$ and $\mathbf{S}$ since for every invertible $n \times n$ matrix (i.e., indexed by the ingredients) $\mathbf{G}$, for the matrices $\mathbf{C}' = \mathbf{CG}^{-1}$ and $\mathbf{S}'^{\mathbf{T}} = \mathbf{GS}^{\mathbf{T}}$ we have

$$\mathbf{R} = \mathbf{CS}^{\mathbf{T}} + \mathbf{E} = \mathbf{CG}^{-1}\mathbf{GS}^{\mathbf{T}} + \mathbf{E} = \mathbf{C}'\mathbf{S}'^{\mathbf{T}} + \mathbf{E}, \tag{8}$$

which will result in a matrix factorization with the same error matrix $\mathbf{E}$ hence error functional $\mathrm{L}(\mathbf{E})$. This non-uniqueness is referred to as rotational ambiguity. Another type of ambiguity, known as intensity ambiguity, can be addressed using normalization. To enhance the likelihood of obtaining unique solutions and ensuring correspondence to the actual chemical system, additional constraints can be applied in MCR-ALS. Two such constraints are non-negativity and the correspondence among species constraints.

The non-negativity constraint ensures that all elements of the concentration matrix $\mathbf{C}$ and the spectral matrix $\mathbf{S}^{\mathrm{T}}$ are non-negative, reflecting the physical reality that concentrations and Reflectance cannot be negative. The correspondence among species constraint is applied when analyzing multiple datasets that share a common mode, generating multi-block data. In this approach, the main dataset (e.g., the trial data) can be linked to additional datasets, such as those obtained from pure binary mixtures. This constraint incorporates prior information about the presence or absence of specific components by defining the number and identity of compounds in each data block. The inclusion of this constraint can significantly enhance the accuracy and reliability of the results by leveraging the shared chemical information across datasets.

A schematic of multiset data structure is presented in Scheme 1. It is important to note that the correspondence among species imposes constraints on the concentration matrix $\mathbf{C}$, specifically forcing certain values to be either zero or non-zero based on prior knowledge of the presence or absence of specific components. This *a priori* information ensures that the decomposition is consistent with known chemical or physical conditions, enhancing the reliability of the resulting profiles. By enforcing these constraints, the method avoids unrealistic component concentrations and ensures that the species are represented accurately across the different datasets. An additional component, denoted as X, is introduced as an additional component, to capture bilinear information that cannot be fully explained by the three main components. By introducing this fourth component, any bilinear contributions—such as noise, background signals, or unmodeled variations—are effectively isolated from the primary chemical components. This enhances the overall decomposition by ensuring that the known components remain more accurately represented, while the unaccounted-for variations are managed separately.

During the alternating least squares (ALS) procedure, the matrix $\mathbf{S}^{\mathrm{T}}$ can be normalized such that the maximum value in each column is set to 1. This greatly restricts the intensity ambiguity. The optimization of these profiles is carried out iteratively using ALS

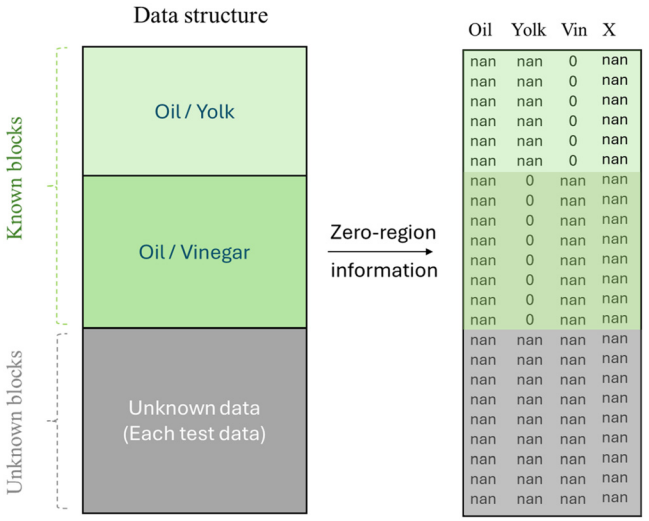

SCHEME 1. The schematic representation of the input data for MCR-ALS analysis. In each trial, the gray section varies, and MCR-ALS decomposes the multiset data accordingly. The process of constraining certain elements of the concentration matrix **C** to be zero or non-zero, based on prior knowledge of species presence or absence, is referred to as the "correspondence among the species" constraint.

until the residual matrix **E**, which accounts for unmodeled sources of variance, is minimized. The quality of the decomposition is evaluated by the lack of fit (LOF%) criterion, which quantifies the difference between the original matrix **R** and the reconstructed matrix $\mathbf{CS}^{\mathrm{T}}$. After deriving the concentration matrices **C** from the MCR-ALS method, the next step involves refolding these matrices to create contribution maps, which allow for the visualization of the spatial distribution of the components. Once the contribution maps are generated, droplet sizes can be calculated. The ultimate objective is to develop a single metric that quantifies the spatial distribution and variability of the components within the sample, providing a comprehensive measure of heterogeneity.

Kullback–Leibler (KL) divergence[23,24] is a measure used to quantify the difference between two probability distributions, indicating the amount of information lost when one distribution approximates another. It is inherently related to information entropy, offering a method to evaluate how one distribution deviates from an expected or baseline distribution. In hyperspectral imaging, KL divergence is employed to assess how the spatial distributions of various components—such as oil, yolk, and vinegar—deviate from a uniform spatial distribution. The goal in a successful emulsion is to achieve a low KL divergence, reflecting a uniform distribution of small, well-dispersed droplets (often smaller than the resolution of the HSI technique). In the case of homogeneous mayonnaise, this implies that the droplets are consistently small and evenly distributed over scales significantly larger than their size. Thus, KL divergence serves as a critical metric for evaluating the uniformity and distributional consistency of the components, analogous to evaluating emulsion quality based on droplet size distribution. The resulting matrix **C** from MCR-ALS was initially normalized such that the sum of the elements in each row equals one. The normalized matrix for each ingredient is called $\boldsymbol{p}_n(x,y)$. Similarly, the mean intensity fraction q_k is computed by averaging over all NM pixels (where N and M denote the number of pixels in the x and y spatial directions, respectively)

$$q_n = \frac{1}{NM}\sum_{(x,y)} \boldsymbol{p}_n(x,y). \tag{9}$$

The degree to which the intensity fractions $p_n(x,y)$ approach the mean value q_n indicates the homogeneity of the sample. This homogeneity can be quantified using the KL divergence from the mean intensity fraction per pixel. For a fixed pixel (x,y), $\boldsymbol{p}_\bullet(x,y) = (p_1(x,y), \ldots, p_N(x,y))$ is a probability distribution over the different ingredients. Likewise, $\boldsymbol{q}_\bullet = (q_1, \ldots, q_N)$ is a probability distribution over the ingredients. We can, therefore, consider the KL divergence between these two distributions, i.e.,

$$KL(x,y) = KL\big(\boldsymbol{p}_\bullet(x,y)\|\boldsymbol{q}_\bullet\big) = \sum\nolimits_n p_n(x,y)\log\left(\frac{p_n(x,y)}{q_n}\right), \tag{10}$$

where the definition of this KL-divergence is spelled out in the last equalities of Eq. (10). A well-known property of KL divergence is that this measure is non-negative and equals zero if and only if $p_k(x,y) = q_k$. The average KL divergence is then defined as

$$KL = \frac{1}{NM}\sum_{(x,y)} KL(x,y) = \sum_{n,(x,y)} \frac{p_n(x,y)}{NM}\log\left(\frac{\frac{p_n(x,y)}{\frac{NM}{n}}}{\frac{NM}{NM}}\right). \tag{11}$$

In this expression, the average divergence is represented as a KL divergence of probability distributions across both the components and the pixels. In the context of successful mayonnaise preparation, the objective is to achieve a stable emulsion where oil droplets are uniformly small and well-dispersed throughout the mixture. This uniformity indicates a well-mixed system with minimal deviation from the ideal state. However, the pixel scale is an arbitrary measure dictated by camera resolution, and homogeneity should be assessed relative to the droplet size. To analyze homogeneity across different scales, we convolve p_n with a kernel, effectively averaging over a local neighborhood of radius r (expressed in units of pixel edges, i.e., 15 μm in the present case). This is expressed as

$$p_n^{(r)}(x,y) = \frac{1}{\#\{(x',y'), |x-x'| \le r, |y-y'| \le r\}} \sum_{\substack{|x'-x| \le r, \\ |y'-y| \le r}} p_n(x',y'), \tag{12}$$

where $\#\{(x', y'), |x - x'| \le r, |y - y'| \le r\}$ denotes the count of pixels (x′,y′) within the local neighborhood of radius r centered at (x,y). The scale-dependent average KL divergence is then calculated as

$$\begin{aligned} KL^{(r)} &= \frac{1}{NM}\sum_{(x,y)} KL^{(r)}(x,y) \\ &= \sum_{n,(x,y)} \frac{p_n^{(r)}(x,y)}{NM}\log\left(\frac{\frac{p_n^{(r)}(x,y)}{NM}}{\frac{q_n}{NM}}\right). \end{aligned} \tag{13}$$

Note that the normalization factor is $(2r+1)^2$ if the neighborhood does not intersect the pixel boundary.

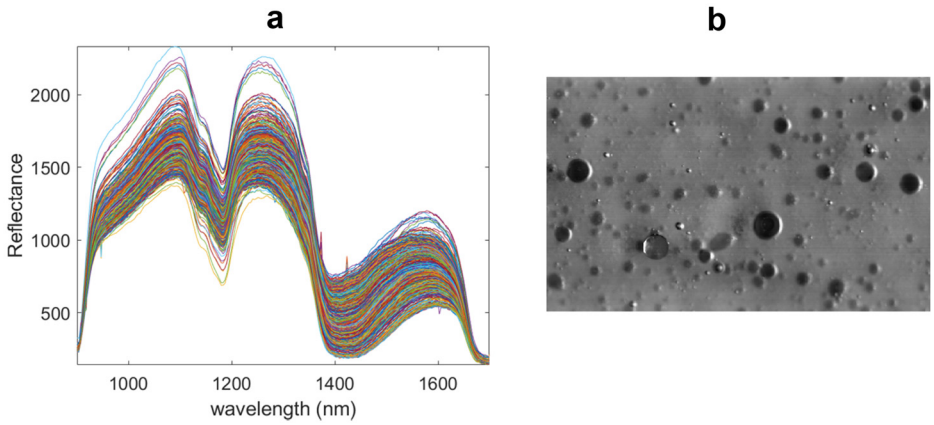

FIG. 4. (a) Raw spectral data and (b) the mean image of the raw data.

III. RESULTS AND DISCUSSION

In this section, the analysis is divided into two parts. First, a single dataset is analyzed to clarify the essential steps outlined in the theory. Then, the analysis is expanded to include all datasets, applying the same principles for broader insights.

A. Single dataset

To begin the results section, we selected the dataset corresponding to trial 4 to illustrate the proposed approach in determining the success or failure of mayonnaise production using chemometrics. The spectral dataset is presented in Fig. 4(a). These spectra generally agree with spectra published previously.[25]

Each profile represents the measured NIR spectra from a single pixel of the sample. The mean image of the same dataset is shown in Fig. 4(b). This image was generated by calculating the mean value of each NIR spectrum and using it as the intensity for the corresponding pixel in the image.

Figure S1(a) displays the logarithm of the eigenvalues (squared singular values) plotted against the number of singular values. The plot demonstrates that most of the data variance is captured by the first three principal components (PCs). Meanwhile, Fig. S1(b) illustrates the first six loadings, with a clear trend in the first three. Beyond the fourth component, the signal becomes dominated by noise rather than meaningful variance. This indicates that mixing does not introduce significant nonlinearities in the spectroscopy data, as it does not result in additional meaningful singular values.

Figure S2 presents the score plot of the data. To facilitate meaningful visualization, we normalize **SC** by its first column, ensuring all elements in the first column equal one. This normalization allows us to plot the second column against the third column of the normalized **SC**, represented by black stars in Fig. S2. This plot helps in visualizing the data distribution and the relationship between different pixels.

Included in Fig. S2 are also the data points representing pure components: yolk, vinegar, and oil. These pure components were obtained from separate pure ingredient datasets. On the plot, the pure ingredient points are located near the edges of the data triangle. This indicates that the pure components are the extreme values in the dataset, while the mixture of these components (the actual experimental data) falls within the bounds of this triangle. The positioning of the pure ingredients at the edges and the mixed ingredients inside the triangle can be understood through the nature of compositional data. In compositional data analysis, each data point (or pixel) represents a mixture of components rather than a single component. Consequently, all pixels in our dataset are mixtures of yolk, vinegar, and oil, and none of the pixels are composed of just a single ingredient. This is evident as no data points are found outside the bounds formed by the pure components.

To facilitate analysis using MCR-ALS, a multiset structure was generated. This multiset structure plays a crucial role in applying constraints related to species correspondence, which ensures a more accurate and unique decomposition of the data. In this process, binary datasets representing the two-component systems—Oil/Yolk and Oil/Vinegar—were concatenated with the mixture data along the column dimension. This multiset, consisting of three submatrices (one for oil/yolk, one for oil/vinegar, and the third corresponding to the dataset of trial 4), was then decomposed using MCR-ALS.

MCR-ALS decomposed the dataset into smaller matrices, **C** and $\mathbf{S}^T$. These matrices provide distinct information about the main ingredients of the mayonnaise: vinegar, oil, and yolk. Specifically, **C** represents the intensity and concentration of these ingredients across different pixels, while $\mathbf{S}^T$ contains their spectral signatures. This bilinear decomposition results in $\mathbf{S}^T$ comprising three spectral profiles, as illustrated in Fig. 5. Subsequently, **C** is refolded to generate the contribution and abundance maps, which are visualized in Fig. 5.

The contribution maps from this experiment likely indicate a failed mayonnaise, specifically a water-in-oil emulsion. The contribution map for oil shows that oil is the continuous phase, encapsulating both vinegar and yolk. The spectral profile of vinegar, as shown in Fig. 5(c), closely resembles the water signature in the NIR spectrum, given that vinegar consists of approximately 93%–96% water.

Consequently, the droplet sizes were subsequently calculated. Initially, an image processing procedure was applied, encompassing contrast enhancement, filtering, and watershed segmentation to quantify droplet size and distribution. The droplet areas are displayed in a histogram to illustrate their size distribution, as shown for trial 4 in Fig. 6.

B. All datasets

The results from a single dataset can be generalized to all experiments. Here, we present a comprehensive analysis. Equation (5) shows

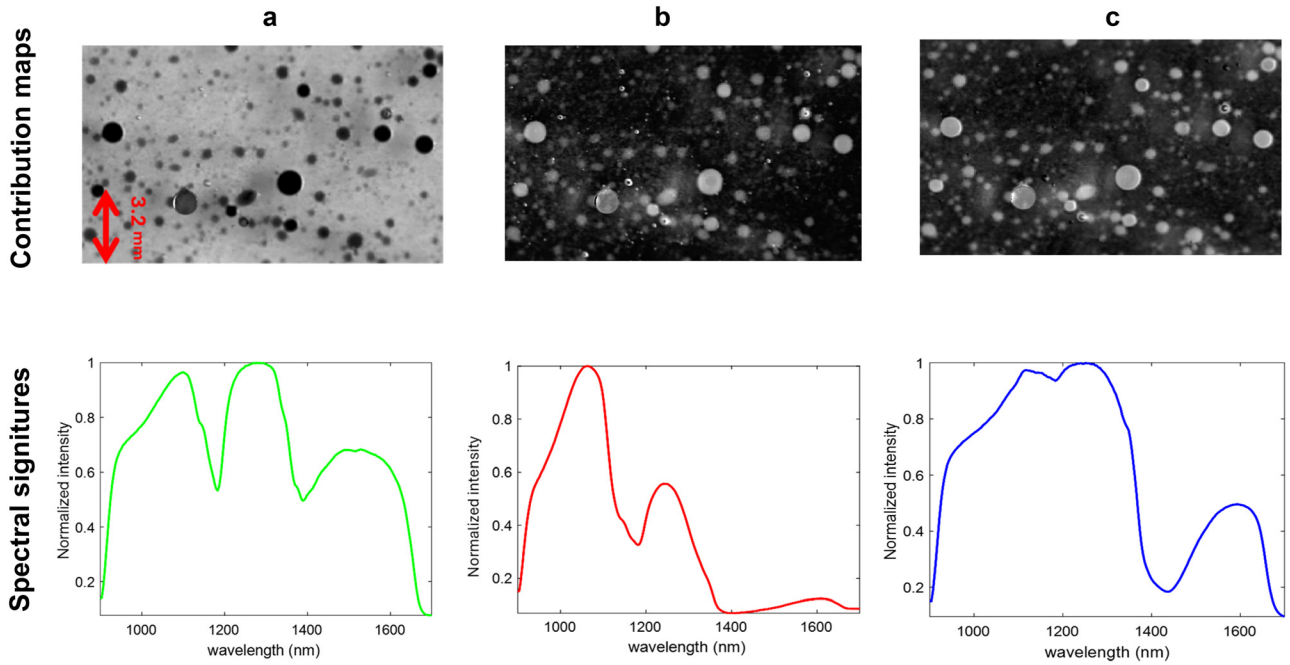

FIG. 5. Contribution maps and spectral signatures of the three main ingredients: (a) oil, (b) yolk, and (c) vinegar—of trial 4, obtained using MCR-ALS.

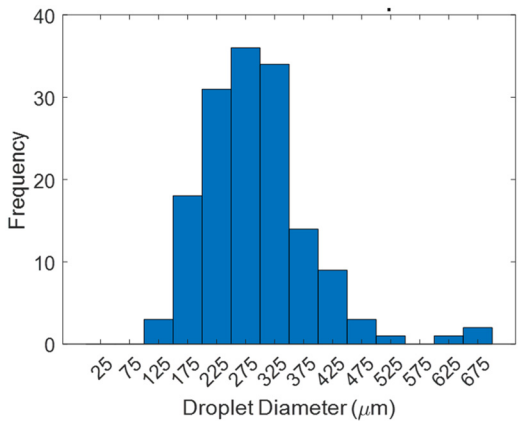

FIG. 6. The droplet diameters in trial 4.

that $\widetilde{\mathbf{R}}$ is unfolded into a matrix **R**. For each trial, we obtain a matrix **R**. Each **R** was then subjected to MCR-ALS with non-negativity constraints and correspondence among the species constraints. Given that **C** and $\mathbf{S}^{\mathrm{T}}$ must be non-negative and considering the inclusion of pure datasets collected from individual ingredients, the constraints enhance the accuracy of the decomposition. The results will include the spectral signatures and the contribution/abundance maps for seven trials, as presented in Figs. 7 and 8. Figure 7 presents the spectral signatures of the three ingredients obtained from the MCR-ALS analysis for seven trials. Each panel in Fig. S3 displays seven spectral profiles, corresponding to the results of the seven different trials. Figure S3 presents the resulting contribution maps.

Based on the resulting contribution maps, Fig. 7, it appears that in the first two trials, vinegar acts as the continuous phase containing oil droplets, indicating the successful formation of an oil-in-water emulsion. It should be noted that for these trials the oil-in-water droplet sizes are expected to be typically smaller than the resolution of the HSI, so the image only shows the large-size tail of the droplet size distribution (also implying that Fig. 2 cannot be used for a prediction of droplet size for the emulsions in trials 1 and 2 that can be quantitatively tested). The remaining trials show oil as the continuous phase, suggesting that these resulted in water-in-oil emulsions, which are considered failures. The presence of large black circles observed in the first two trials appears to be attributable to air bubbles introduced into the solution during the stringing or mixing process.

Subsequently, the droplet sizes were computed using the previously described methodology, and the results are presented in Fig. 8. This figure illustrates the diameter distribution of droplets across seven trials. The box plot in Fig. 8(a) shows that droplet sizes are smaller in the first two trials (trials 1 and 2) and the last trials (trials 6 and 7) compared to the intermediate trials (trials 3 to 5), which display larger droplet sizes. In Fig. 8(a), circles denote individual data points that fall outside the typical range of the dataset. Filled circles indicate mild outliers, which are data points that lie beyond 1.5 times the interquartile range (IQR) from the quartiles but within three times the IQR. Empty circles represent more extreme outliers, falling beyond three times the IQR. These visual markers assist in identifying and analyzing deviations from the central data distribution. Notably, there is a distinct discontinuity between the second and third trials, with the mean droplet size increasing from 100 to 240 μm, which indicates the phase inversion point where the emulsion type transitions from oil-in-water to water-in-oil. This discontinuity highlights the critical influence of

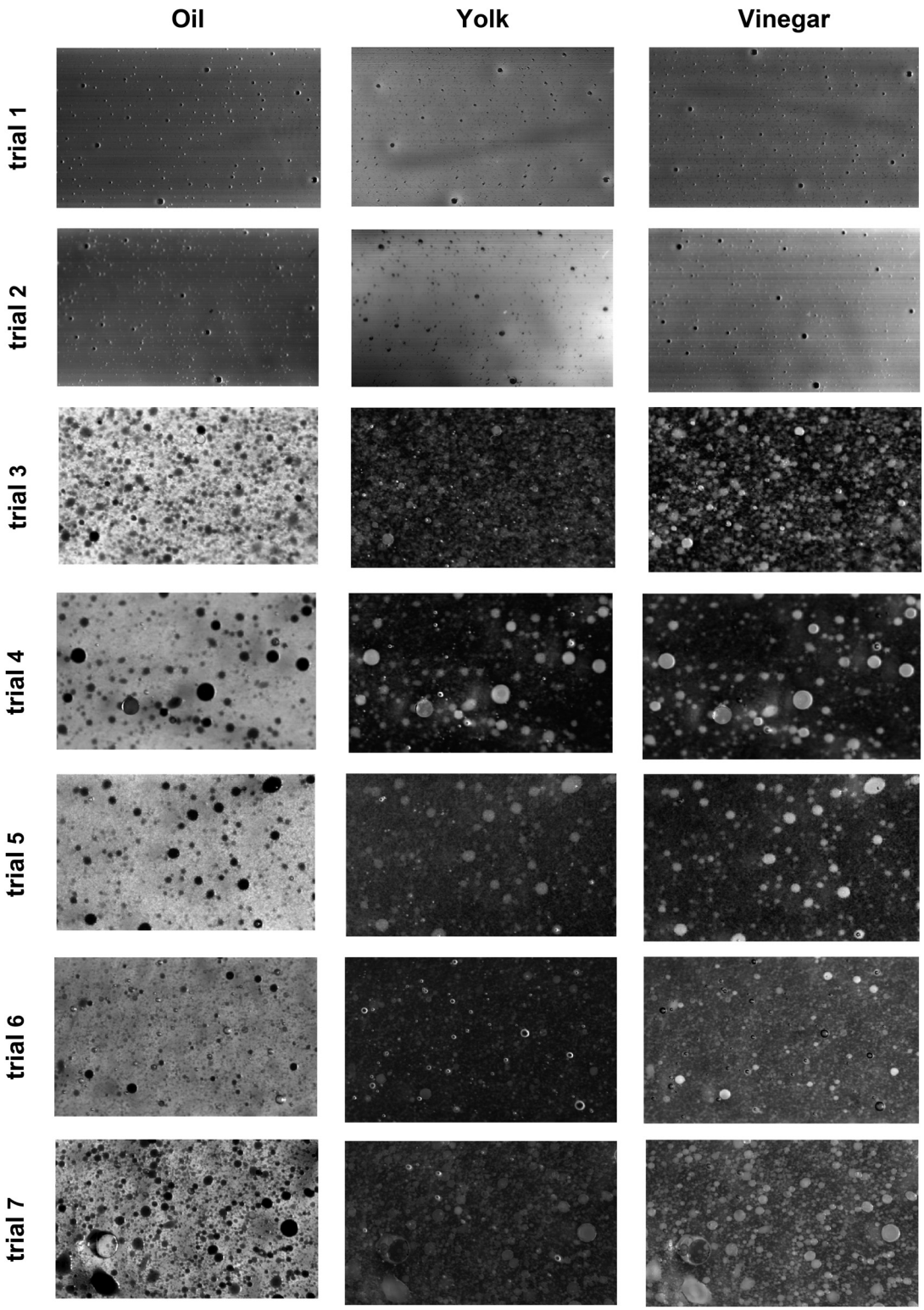

FIG. 7. The resulted contribution maps of three ingredients, oil, yolk, and vinegar in seven trials by MCR-ALS, are presented. The intensity values in these maps range from 0 (black) to 1 (white), corresponding to the pixel values in the images.

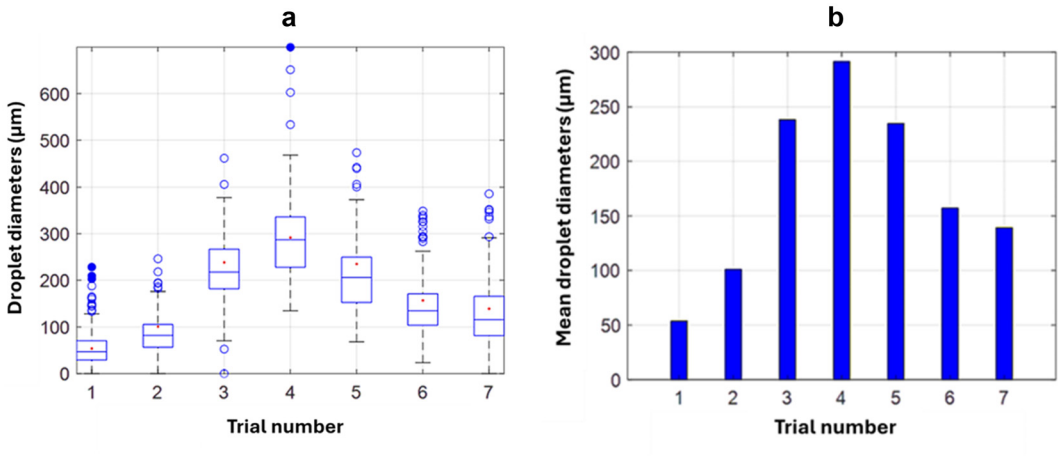

FIG. 8. (a) Box plot showing the diameter distribution of droplets across seven trials, highlighting the phase inversion between the second and third trials. (b) Mean droplet sizes for each trial.

experimental conditions on droplet size distribution. Meanwhile, Fig. 8(b) presents the mean droplet sizes for each trial.

Figure 9 presents the KL divergence, $KL^{(r)}$ computed for each of the seven trials across five distinct *r* levels. The plot reveals a significant discontinuity between the KL divergence values of trials1 and 2 compared to the other trials. The initial two trials exhibit the smallest and finest oil droplets (as shown in Fig. 7) and consequently display the lowest $KL^{(r)}$ values across all *r* levels. In contrast, trials 4 and 5 show the highest $KL^{(r)}$ values at all *r* levels, indicating that these experiments are the furthest from achieving homogeneity and contain larger droplet sizes. Although the $KL^{(r)}$ values decrease for all trials, the reduction is most pronounced for trials 4 and 5. This discontinuity suggests the presence of a phase inversion point, where the characteristics of the emulsion undergo a significant transformation between trials 2 and 3. This shift likely marks a transition in the structure of the emulsion, indicating a change from a state with smaller, more uniformly distributed oil droplets to one with larger droplets and less homogeneity.

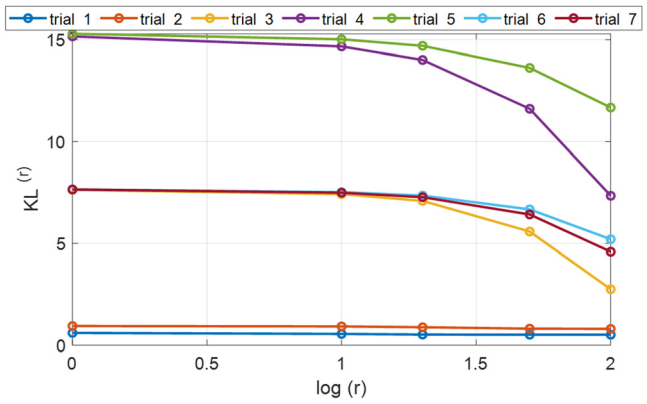

FIG. 9. After generating the **C** matrices from MCR-ALS for seven trials, the Kullback–Leibler divergence $KL^{(r)}$ was calculated for five r values and is presented as a function of log(r).

Prior to this point, the mayonnaise appears to form a stable oil-in-water emulsion, where oil droplets are dispersed within the aqueous phase, indicating successful emulsion formation. However, beyond this transition point, the emulsion appears to shift to a water-in-oil system, where water droplets are dispersed within the oil phase, signaling a failed emulsion. The maximum percentage of added oil in the egg yolk+oil mixture that still allows the oil to be mixed in homogeneously in the oil-in-water emulsion is in the range of 33%–50%. This confirms that mixing does not proceed well in relatively large pools of oil, as mentioned in the Introduction. The observed phase inversion is critical as it underscores the influence of experimental conditions on the stability and type of emulsion formed, thereby impacting the quality of the mayonnaise. This discontinuity in KL divergence provides a quantitative measure of this shift, offering valuable insight into the behavior of emulsions under varying conditions and aiding in the optimization of mayonnaise production processes.

IV. CONCLUSIONS

Hyperspectral imaging (HSI) is a sophisticated noninvasive technique that captures both spatial and spectral data, offering detailed insights into material properties. In this study, we utilized near infrared (NIR) hyperspectral imaging with the SPECIM FX17 camera, equipped with a macro lens, to achieve high spectral resolution and precise spatial differentiation over the 900–1700 nm range. This setup proved highly effective for analyzing mixing phenomena in concentrated oil-in-water (o/w) and water-in-oil (w/o) emulsions, using mayonnaise as a case study. By combining this advanced spectroscopic technique with detailed image analysis (introducing the Kullback–Leibler divergence metric), we were able to conduct a noninvasive, quantitative evaluation of mixing dynamics, underscoring the broader applicability of spectral imaging technologies in fluid mechanics, particularly for studying slow mixing processes. To the best of our knowledge, the KL divergence metric has not previously been applied to quantify sample inhomogeneity in image analysis. The findings of this study aim to facilitate the future implementation of noninvasive, real-time monitoring methods in industrial production processes. Such advancements could reduce processing times, prevent failed pre-

emulsions, enhance operational efficiency, and minimize waste, in situations when the mixing process often cannot be checked visually directly.

While this study demonstrates the effectiveness of NIR HSI combined with the Kullback–Leibler divergence metric for tracking emulsion mixing dynamics, alternative techniques like coherent anti-stokes Raman scattering (CARS) could achieve noninvasive analysis without the need for labeling too. A potential advantage of CARS-based techniques is that potentially higher resolutions can be achieved, leading to insights on smaller length scales. However, in the context of future applications of the technique, it is important that NIR-based techniques have a proven track record of use in industrial environments. Together, these methods underscore the potential of advanced spectroscopic tools to investigate emulsion quality control in diverse settings.

A practical implementation of the technique could involve the development of a sensor that acts as a strip photography camera (cf. cameras that capture the photo finish at sport events) for a pre-emulsion that flows past the sensor in an industrial production process. This would create a sensor that directly measures spatial variation inhomogeneity, as opposed to sensors that would derive such information from the variation of the signal over time. The current results suggest that a good quality line image can be obtained in $\sim$10 ms, with room for further optimization by balancing the image resolution and quality against the acquisition time. One would obtain a hyperspectral image reflecting the inhomogeneity in one (spatial) direction and time in the other direction, instead of in two spatial directions as presented in this study. The image analysis would require a modest modification of the data analysis technique above (as the inhomogeneity data are essentially one-dimensional with a strip photography camera). Also, the flow speeds would still be relatively limited: if the inhomogeneities are expected to be of the order of 100 μm, the acceptable flow speeds would be of the order of 10 mm/s, but again, it is expected that there is ample room for optimization of the technique and the present experiment was intended as a first assessment of the feasibility of such an approach.

The analysis reveals that phase inversion from an oil-in-water to a water-in-oil emulsion occurs if oil is added too rapidly during mayonnaise preparation, as indicated by droplet size measurements and KL divergence results showing a discontinuity between the second and third trials. This finding underscores the importance of achieving a precise balance for stable emulsions, focusing on interfacial tension and phase behavior. Practically, this means that accurate ingredient proportions and mixing techniques are crucial for achieving desired emulsion properties in culinary applications. By integrating chemometrics with NIR spectral data and droplet size measurements, this study connects theoretical principles with practical applications, offering valuable insights for optimizing emulsion processes and enhancing food quality and consistency.

However, the results do not suggest that home chefs need to invest in an HSI set up to prepare the perfect mayonnaise. Ultimately, patience remains the most essential ingredient.

SUPPLEMENTARY MATERIAL

See the supplementary material for figures showing a number of intermediate steps in the data analysis procedure: Figure S1(a) displays the logarithm of the eigenvalues (squared singular values) plotted against the number of singular values; Fig. S1(b) illustrates the first six loadings; Fig. S2 presents the score plot of the data; and Fig. S3 presents the resulting contribution maps.

ACKNOWLEDGMENTS

This project was co-funded by TKI-E&I with the supplementary grant "TKI-Toeslag" for Topconsortia for Knowledge and Innovation (TKI's) of the Ministry of Economic Affairs and Climate Policy. The authors thank all partners within the project "Measurement for Management (M4M)" (https://ispt.eu/projects/m4m/), managed by the Institute for Sustainable Process Technology (ISPT) in Amersfoort, The Netherlands.

AUTHOR DECLARATIONS

Conflict of Interest

The authors have no conflicts to disclose.

Author Contributions

Mahdiyeh Ghaffari: Conceptualization (equal); Data curation (equal); Investigation (equal); Visualization (equal); Writing – original draft (equal); Writing – review & editing (equal). **Arjen Bot:** Writing – review & editing (equal). **Rogier Brussee:** Writing – review & editing (equal). **Gerjen H. Tinnevelt:** Writing – review & editing (equal). **Jeroen J. Jansen:** Funding acquisition (equal); Writing – review & editing (equal).

DATA AVAILABILITY

The data that support the findings of this study are available from the corresponding author upon reasonable request.

REFERENCES

[1]H. McGee, *On Food and Cooking: The Science and Lore of the Kitchen* (Scribner, 2007).
[2]I. M. Krieger and T. J. Dougherty, "A mechanism for non-Newtonian flow in suspensions of rigid spheres," Trans. Soc. Rheol. **3**(1), 137–152 (1959).
[3]B. J. Bentley and L. G. Leal, "An experimental investigation of drop deformation and breakup in steady, two-dimensional linear flows," J. Fluid Mech. **167**, 241–283 (1986).
[4]D. W. de Bruijne and A. Bot, *Fabricated Fat-Based Foods, in Food Texture: Measurement and Perception*, edited by A. J. Rosental (Aspen Publishers, 1999), Chap. 7, pp. 185–227.
[5]A. Bot, E. Flöter, H. P. Karbstein-Schuchmann, and H. Santos-Ribeiro, "Emulsion gels in foods," in *Product Design and Engineering: Formulation of Gels and Pastes*, edited by U. Bröckel, W. Meier, and G. Wagner (Wiley-VCH Verlag, 2013), Chap. 11, pp. 315–342.
[6]H. P. Grace, "Dispersion phenomena in high viscosity immiscible fluid systems and application of static mixers as dispersion devices in such systems," Chem. Eng. Commun. **14**(3–6), 225–277 (1982).
[7]A. Bhargava *et al.*, "Hyperspectral imaging and its applications: A review," Heliyon **10**(12), e33208 (2024).
[8]D.-W. Sun, H. Pu, and J. Yu, "Applications of hyperspectral imaging technology in the food industry," Nat. Rev. Electr. Eng. **1**(4), 251–263 (2024).
[9]C. B. Karaziack *et al.*, "Application of near-infrared hyperspectral imaging for determination of cheese chemical composition," J. Food Compos. Anal. **127**, 105994 (2024).
[10]A. De Juan, J. Jaumot, and R. Tauler, "Multivariate curve resolution (MCR). Solving the mixture analysis problem," Anal. Methods **6**(14), 4964–4976 (2014).
[11]M. Greenacre *et al.*, "Principal component analysis," Nat. Rev. Methods Primers **2**(1), 100 (2022).

[12]J. Jia *et al.*, "Status and application of advanced airborne hyperspectral imaging technology: A review," Infrared Phys. Technol. **104**, 103115 (2020).
[13]X. Dong *et al.*, "A review of hyperspectral imaging for nanoscale materials research," Appl. Spectrosc. Rev. **54**(4), 285–305 (2019).
[14]A. Baiano, "Applications of hyperspectral imaging for quality assessment of liquid based and semi-liquid food products: A review," J. Food Eng. **214**, 10–15 (2017).
[15]R. Bhargava and K. Falahkheirkhah, "Enhancing hyperspectral imaging," Nat. Mach. Intell. **3**(4), 279–280 (2021).
[16]A. Dashti *et al.*, "Comparison of a portable Vis-NIR hyperspectral imaging and a snapscan SWIR hyperspectral imaging for evaluation of meat authenticity," Food Chem.: X **18**, 100667 (2023).
[17]Y. Zhang *et al.*, "In situ detection of moisture content and gelatinization degree during rice processing using hyperspectral imaging," J. Food Compos. Anal. **130**, 106172 (2024).
[18]Y. Zhao *et al.*, "Visible/near-infrared spectroscopy and hyperspectral imaging facilitate the rapid determination of soluble solids content in fruits," Food Eng. Rev. **16**, 470–496 (2024).
[19]G. Tejasree and L. Agilandeeswari, "An extensive review of hyperspectral image classification and prediction: Techniques and challenges," Multimedia Tools Appl. **83**, 80941–80998 (2024).
[20]R. L. Carneiro and R. J. Poppi, "Infrared imaging spectroscopy and chemometric tools for in situ analysis of an imiquimod pharmaceutical preparation presented as cream," Spectrochim. Acta, Part A **118**, 215–220 (2014).
[21]S. S. Vijayashekhar, V. S. Deshpande, and J. S. Bhatt, "A practical approach for hyperspectral unmixing using deep learning," IEEE Geosci. Remote Sens. Lett. **19**, 1–5 (2022).
[22]A. de Juan and R. Tauler, "Multivariate curve resolution: 50 years addressing the mixture analysis problem–A review," Anal. Chim. Acta **1145**, 59–78 (2021).
[23]M. Basseville, "Divergence measures for statistical data processing—An annotated bibliography," Signal Process. **93**(4), 621–633 (2013).
[24]Y. Zhang, J. Pan, K. Li, W. Liu, Z. Chen, X. Liu, and J. Wang, "On the properties of Kullback-Leibler divergence between multivariate Gaussian distributions," in *Advances in Neural Information Processing Systems*, edited by A. Oh, T. Naumann, A. Globerson, K. Saenko, M. Hardt, and S. Levine (Curran Associates, Inc., 2023), Vol. 36, pp. 58152–58165.
[25]P. Mishra *et al.*, "At-line and inline prediction of droplet size in mayonnaise with near-infrared spectroscopy," Infrared Phys. Technol. **123**, 104155 (2022).